EXTENDED PDF FORMAT
SPONSORED BY
Stem Cell Marker Antibodies
>Learn More
R&D SYSTEMS
www.rndsystems.com

Science AAAS

The Role and Implications of Bassanite as a Stable Precursor Phase to Gypsum Precipitation

A. E. S. Van Driessche *et al.*

Science **336**, 69 (2012);
DOI: 10.1126/science.1215648

This copy is for your personal, non-commercial use only.

If you wish to distribute this article to others, you can order high-quality copies for your colleagues, clients, or customers by clicking here.

Permission to republish or repurpose articles or portions of articles can be obtained by following the guidelines here.

The following resources related to this article are available online at www.sciencemag.org (this information is current as of August 11, 2013):

Updated information and services, including high-resolution figures, can be found in the online version of this article at:
http://www.sciencemag.org/content/336/6077/69.full.html

Supporting Online Material can be found at:
http://www.sciencemag.org/content/suppl/2012/04/04/336.6077.69.DC1.html

This article **cites 31 articles**, 7 of which can be accessed free:
http://www.sciencemag.org/content/336/6077/69.full.html#ref-list-1

This article has been **cited by** 2 articles hosted by HighWire Press; see:
http://www.sciencemag.org/content/336/6077/69.full.html#related-urls

This article appears in the following **subject collections:**
Geochemistry, Geophysics
http://www.sciencemag.org/cgi/collection/geochem_phys
Materials Science
http://www.sciencemag.org/cgi/collection/mat_sci

Science (print ISSN 0036-8075; online ISSN 1095-9203) is published weekly, except the last week in December, by the American Association for the Advancement of Science, 1200 New York Avenue NW, Washington, DC 20005. Copyright 2012 by the American Association for the Advancement of Science; all rights reserved. The title *Science* is a registered trademark of AAAS.

The Role and Implications of Bassanite as a Stable Precursor Phase to Gypsum Precipitation

A. E. S. Van Driessche,[1] L. G. Benning,[2]* J. D. Rodriguez-Blanco,[2] M. Ossorio,[1,2] P. Bots,[2] J. M. García-Ruiz[1]*

Calcium sulfate minerals such as gypsum play important roles in natural and industrial processes, but their precipitation mechanisms remain largely unexplored. We used time-resolved sample quenching and high-resolution microscopy to demonstrate that gypsum forms via a three-stage process: (i) homogeneous precipitation of nanocrystalline hemihydrate bassanite below its predicted solubility, (ii) self-assembly of bassanite into elongated aggregates co-oriented along their *c* axis, and (iii) transformation into dihydrate gypsum. These findings indicate that a stable nanocrystalline precursor phase can form below its bulk solubility and that in the $CaSO_4$ system, the self-assembly of nanoparticles plays a crucial role. Understanding why bassanite forms prior to gypsum can lead to more efficient anti-scaling strategies for water desalination and may help to explain the persistence of $CaSO_4$ phases in regions of low water activity on Mars.

The precipitation of calcium sulfate phases (gypsum, bassanite, and anhydrite) from seawater led to the formation of numerous ancient and modern evaporite deposits on Earth (*1*, *2*) and to abundant gypsum (*3*) and bassanite (*4*) on Mars. Today the precipitation of gypsum poses a serious economic threat through the formation of massive mineral scales in pipes and other production equipment in desalination plants that produce drinking water (*5*, *6*). The formation of gypsum ($CaSO_4•2H_2O$) from solution is generally assumed to proceed via a single-step direct precipitation pathway (*7*), although a multistep pathway including an amorphous intermediate (*8*) has been reported. One current limitation in quantifying and controlling this reaction is the lack of a mechanistic understanding of the stages and variations in the structural identities of the solids that form during gypsum synthesis.

Using two fast solution sample-quenching methods [vacuum/solvent filtration (*9*) and cryo-quenching (*10*)] and high-resolution transmission electron microscopy (HR-TEM), we investigated the early stages of the nucleation and growth process(es) leading to the precipitation of $CaSO_4$ phases (*11*). We performed precipitation experiments in solutions supersaturated with respect to gypsum (saturation index $SI_{Gyp} = +0.14$ to $+1.04$) (*11*) in order to mimic typical precipitation conditions in desalination plants and in natural evaporitic environments (e.g., saline lakes), which ultimately play a decisive role in controlling the global sulfur cycle.

The first reaction observed was the homogeneous nucleation of nanocrystal particles 10 to 15 nm in diameter, with a *d*-spacing of 6.0 ± 0.2 Å ($n = 80$) (Fig. 1, A and B). Among all possible calcium sulfate phases (*12*, *13*), this *d*-spacing is characteristic of only the hemihydrate bassanite ($CaSO_4•0.5H_2O$). Remarkably, the bassanite nanocrystals nucleated at undersaturated conditions ($SI_{Bas} = -0.02$ to -0.72) (*11*). We confirmed their presence through fast Fourier transform (FFT) measurements (Fig. 1A, inset) of many individual particles and through selected area electron diffraction (SAED) of bassanite nanoparticle areas (Fig. 1G). Furthermore, the cryo-quench technique showed that these nanocrystals are not sample preparation artifacts. Images of nanoparticles produced using this approach revealed identical bassanite nanocrystals, also with the 6.0 Å and 3.48 Å *d*-spacings typical of bassanite (Fig. 1B). Finally, the presence of bassanite at these early stages was confirmed through powder x-ray diffraction of bulk samples extracted from the reacting solutions via different vacuum/solvent filtration techniques (fig. S1).

Once nucleated, these initially rounded nanoparticles seemed to be stable relative to the solution for short periods of time, after which they grew mainly along their *c* axis, evolving into variably sized nanorods (Fig. 1, C to E, and fig. S2). However, all nanorods maintained the bassanite *d*-spacings, as confirmed by multiple FFT measurements (Fig. 1D, inset) and SAED (Fig. 1H) analyses. The nanorods developed a porous aspect (Fig. 1, C to F) not observed in the >80 bassanite nanoparticles we analyzed (e.g., Fig. 1, A and B). Using a tilt series approach (5° angle per step over a 90° range), we repeatedly imaged various bassanite nanorods and confirmed that the observed porosity was not a consequence of the HR-TEM imaging. Pores 2 to 30 nm in diameter were previously reported in large (50 to 300 μm) bassanite crystals (*14*). Bassanite nanorods grew up to 100 nm in length (Fig. 1, D and E) but ultimately self-assembled into aggregates primarily co-oriented along the *c* axis (Fig. 1F and Fig. 2A). However, all individual nanorods within the oriented aggregates still maintained the bassanite nanostructure, as confirmed by SAED (Fig. 1I).

Finally, the oriented bassanite aggregates (Fig. 2A) transformed into micrometer-sized, well-faceted, thin gypsum crystals (Fig. 2B; corresponding SAED pattern in Fig. 2C). When we imaged these large gypsum crystals at high resolution, remnants of bassanite nanorods (Fig. 2F) and assorted bassanite and gypsum *d*-spacings (Fig. 2, F and G) were still evident. Remnant bassanite was also confirmed through the SAED pattern collected from the large gypsum crystal shown in Fig. 2D, which revealed a combined bassanite (akin to the oriented aggregated bassanite in Fig. 1I) and gypsum reciprocal lattice (Fig. 2E).

These time-resolved observations show that the formation of bassanite nanocrystals and nanorods at undersaturated conditions and their oriented self-assembly are the crucial steps controlling gypsum formation from aqueous solutions. In many other similar salt systems, precipitation from solution proceeds via an amorphous precursor and other metastable crystalline intermediates, all of which form above their bulk solubility [i.e., amorphous calcium carbonate (*15*, *16*), vaterite (*9*), and amorphous calcium phosphate (*16*, *17*)]. Recently, a similar pathway was suggested in which an amorphous calcium sulfate and hemihydrate are sequentially precipitated prior to gypsum formation (*8*). However, our data show that the crystallization of gypsum does not proceed via an amorphous stage, but occurs via the solution-based nucleation, growth, and oriented self-assembly of nanocrystalline bassanite, which precipitates within its "forbidden" undersaturated solubility region ($SI_{Bas} = -0.02$ to -0.72). Such a reaction chain suggests that at ambient conditions, a different pathway for the precipitation of phases from solution and their transformation through the Ostwald rule may be important. Combined with the observation that the hemihydrate (bassanite) precipitated as a precursor to the more hydrated phase (gypsum), these findings contradict the generally accepted bulk solubility behavior (*7*, *13*) for calcium sulfates. Bulk bassanite is metastable across the whole temperature range (Fig. 3A and fig. S3). However, our data reveal bassanite nanoparticles and nanorods that are stable relative to an undersaturated solution (Fig. 3B and fig. S3) (*11*), which suggests that the solubility of the bassanite nanocrystals must be much lower relative to bulk bassanite. Furthermore, at the lowest supersaturation

Online
View slideshow at http://scim.ag/slide_6077.

---

[1] Laboratorio de Estudios Cristalográficos, Instituto Andaluz de Ciencias de la Tierra, Consejo Superior de Investigaciones Cientificas–Universidad de Granada, Av. de las Palmeras 4, 18100 Granada, Spain. [2] School of Earth and Environment, University of Leeds, Leeds LS2 9JT, UK.

*To whom correspondence should be addressed. E-mail: l.g.benning@leeds.ac.uk (L.G.B.); jmgruiz@ugr.es (J.M.G.-R.)

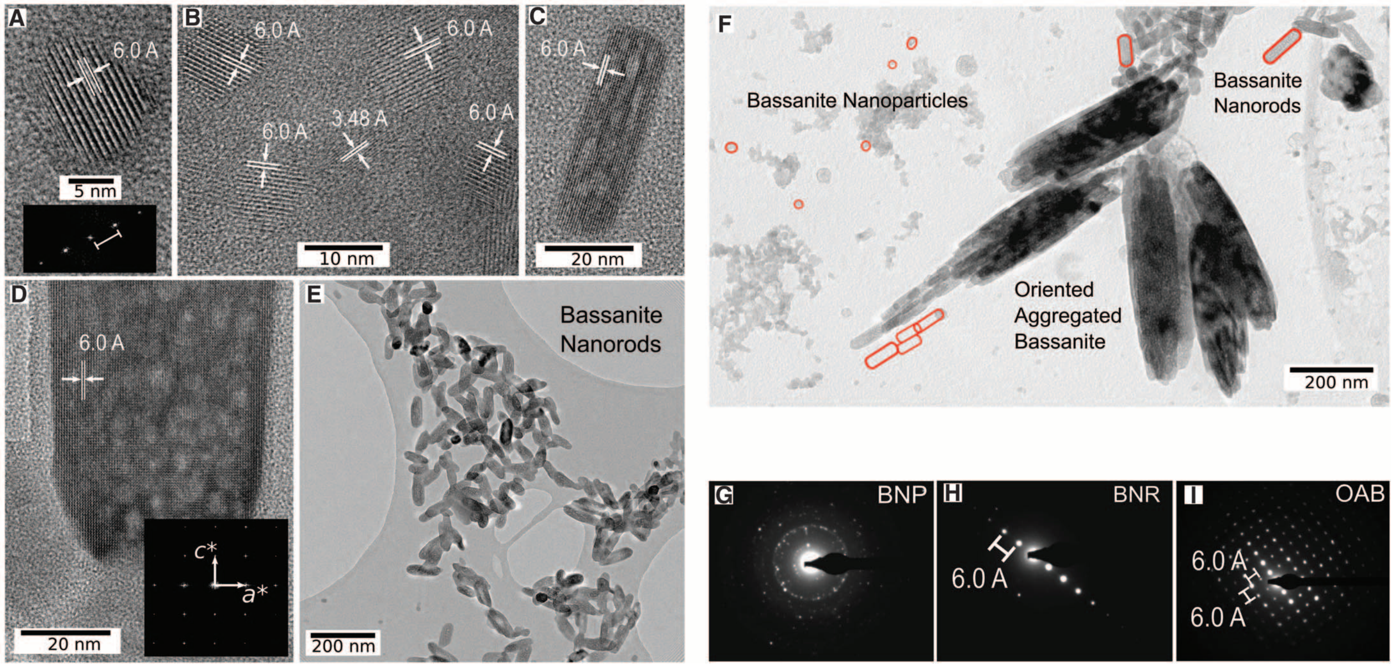

Fig. 1. HR-TEM microphotographs of the first two stages of gypsum crystallization with samples prepared by either fast vacuum/solvent filtration (V/SF) or cryo-quenching (C-Q). (**A**) Typical nanocrystalline bassanite particle (10 s, 100 mM, V/SF) with corresponding FFT of the reciprocal bassanite *d*-spacing along the *a* axis (inset). (**B**) Set of nanoparticles (2 min, 75 mM, C-Q) with the characteristic 6.0 and 3.48 Å *d*-spacings for bassanite. (**C** and **D**) Small and large bassanite nanorods (4 min, 50 mM, V/SF); the inset in (D) shows the FFT corresponding to the reciprocal bassanite two-dimensional lattice structure along the *a* and *c* axes. (**E**) Bassanite nanorods prior to oriented aggregation (15 s, 150 mM, V/SF). (**F**) Oriented bassanite aggregates coexisting with individual bassanite nanorods and bassanite nanoparticles (30 s, 100 mM). Some of the single and co-oriented nanorods are decorated with red ellipsoids for ease of viewing; bassanite nanoparticles are circled in red to highlight their position (not their size). (**G**) SAED pattern of bassanite nanoparticles. (**H**) SAED pattern of bassanite nanorods with the reciprocal lattice along the *c* axis. (**I**) SAED pattern of oriented aggregated bassanite showing the reciprocal lattice along the *a* and *c* axes.

($SI_{Bas} = -0.72$, $SI_{Gyp} = +0.14$; fig. S2B), only small and poorly formed bassanite nanorods were observed, and no gypsum formed even after 24 hours; these findings indicate that when small particles prevail, the solubility of bassanite may actually be lower than that of gypsum.

Similar trends have been observed in several other systems [e.g., alumina (*18*), titania (*19*), and SiO_2 (*20*)], where size- and polymorph-dependent enthalpies play the dominant role in defining phase stability (*21*). This is believed to be a consequence of the small differences in transformation enthalpies between polymorphs (*21*). Furthermore, when nanocrystalline particles become thermodynamically favored and form at the expense of the bulk phase [e.g., ZnS (*22*)], a change in surface enthalpy (energy) with particle size (or surface area) infers a correlation between phase stability (or metastability) and crystal size (*21*, *22*). In the case of gypsum and bassanite, the transformation enthalpy [$\Delta_r H^{\circ}_{\text{Bas-Gyp}} \approx 17$ kJ/mol (*11*)] is comparable to that of other systems. The surface enthalpies of calcium sulfates are much lower than those of other highly crystalline phases [e.g., titania or zirconia (*21*)]. Nonetheless, for our system, the use of a constant surface enthalpy reveals a crossover between gypsum and bassanite only at very small particle sizes (Fig. 3C) (*11*). When variable surface enthalpies are inferred (Fig. 3C) (*23*), a much more realistic picture emerges. The assumption of a direct link between decreasing surface energy and decreasing particle size due to lattice contraction (*23*) leads to a crossover between gypsum and bassanite at a realistic particle size (Fig. 3C) (*11*), but this approach does not account for the formation of bassanite nanocrystals below their bulk solubility.

An alternative concept that construes surface enthalpy as variable (*11*, *22*) better represents our observations of bassanite precipitation below its bulk solubility, yet it assumes an effective negative surface energy for the bulk phase (*22*). Although this is less representative of the conditions in our experiments, it still links the observed bassanite particle size with the oriented aggregation and self-assembly process in several ways: (i) Bassanite nanoparticle nucleation and growth to nanorods occurs when $\Delta_r H^{\circ}_{\text{Bas}}$ decreases with decreasing surface area (i.e., nanoparticles and/or nanorods are thermodynamically favored); (ii) oriented aggregation of the bassanite nanorods occurs when $\Delta_r H^{\circ}_{\text{Bas}}$ increases with decreasing surface area, hence the growth of bassanite from solution becomes thermodynamically unfavorable as $\Delta_r H^{\circ}_{\text{Bas}}$ increases for larger particles; and (iii) the transformation of bassanite to gypsum occurs only when the overall size of the bassanite aggregates causes $\Delta_r H^{\circ}_{\text{Gyp}}$ to become lower than $\Delta_r H^{\circ}_{\text{Bas}}$ (Fig. 3C). Furthermore, the aggregation through oriented self-assembly imparts a morphological control that ultimately leads to the recrystallization to large gypsum crystals. Lastly, the fact that the hemihydrate bassanite transforms to the dihydrate gypsum indicates that water [structural (*24*) and/or bulk] must play an important role in both the self-assembly of the bassanite nanorods and their ultimate transition to gypsum.

On a practical level, these findings show that a different reaction pathway could be responsible for the formation of the massive gypsum deposits in terrestrial evaporitic environments (*1*, *2*) or giant gypsum crystals formed in caves (*25*, *26*) and that this same pathway may also be the reason for the persistence of bassanite in environments with low water activity postulated for Mars (*3*, *4*). Special attention should be paid to the bassanite precursor phase in water desalination plants, as this may help to reduce gypsum scaling. Finally, our results provide a first step to a likely alternative and more cost-effective pathway for bassanite formation at room temperature; currently ~10^{11} kg of bassanite per year are produced for construction purposes ["plaster of Paris" (*7*)] via the thermal dehydration of gypsum, and a direct aqueous synthesis of bassanite at room temperature would avoid the energy cost of high-temperature dehydration (*7*).

Fig. 2. Stage three of the gypsum crystallization reaction. (**A**) Large oriented aggregate with an overall gypsum morphology but formed by self-assembly of bassanite nanorods (15 s, 150 mM, V/SF), with inset showing a detail of the tip section, decorated with red ellipsoids for ease of viewing. (**B** to **E**) Large, highly crystalline gypsum crystals (40 s, 100 mM, V/SF) are shown in (B); a circle marks the area for the corresponding SAED pattern in (C). Gypsum crystals (6 min, 75 mM, C-Q) are shown in (D); a circle marks the area for the SAED pattern in (E). (**F** and **G**) High-resolution images of (D) with marked distances for bassanite (6.0, 3.4, and 3.1 Å) and gypsum (3.1 and 2.8 Å).

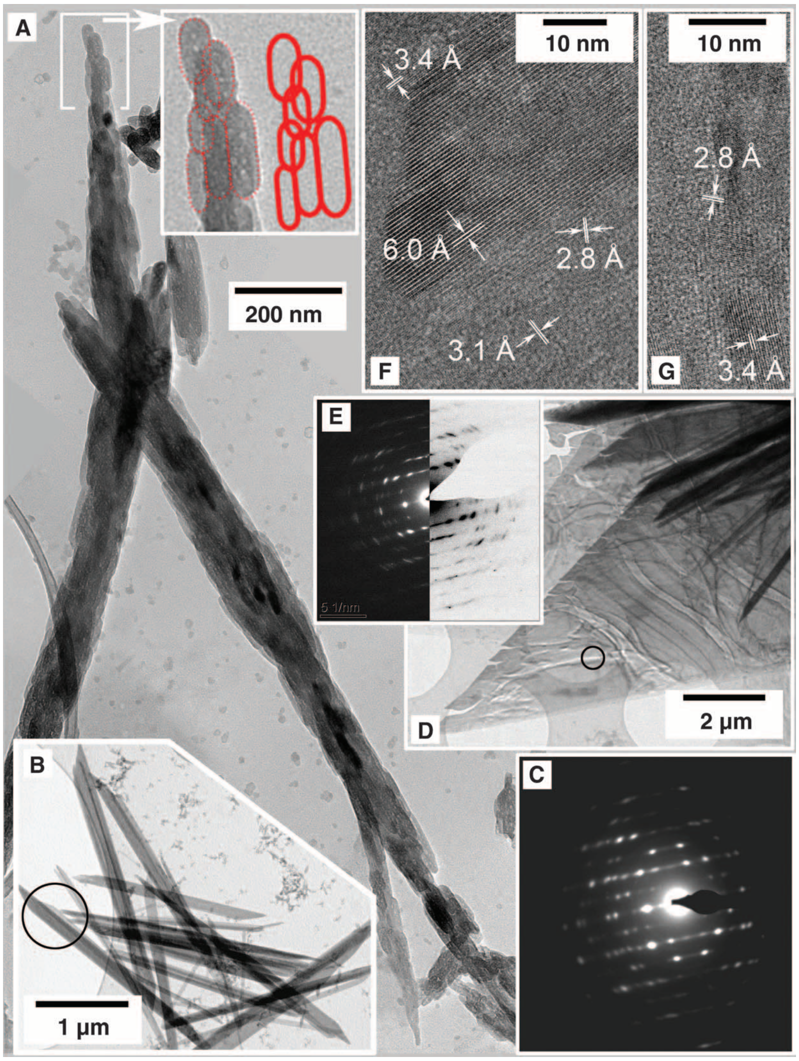

Fig. 3. (**A**) Temperature-dependent solubility diagram for the three $CaSO_4$ polymorphs in pure water at saturated water vapor pressure, with the stable polymorph indicated by solid lines. (**B**) Bulk solubility of bassanite and gypsum calculated at 21°C as a function of total experimental salinity (black dots) with corresponding SI values. The solubility curves, and SI_{Bas} and SI_{Gyp} were calculated with PHREEQC (*11*, *23*). (**C**) Illustration of the link between surface area (or particle size) and enthalpy of reaction (Δ_rH°) with respect to bulk gypsum. The change in enthalpy has been calculated in three ways: (i) using a constant surface energy γ (*18*, *21*) shown with black (gypsum) and red (bassanite) lines, (ii) considering a decreasing surface energy (*23*) with decreasing particle size due to lattice contraction for bassanite nanoparticles (pink curve), and (iii) applying a surface area–dependent surface enthalpy and negative surface energy for bulk bassanite (*22*) shown by the blue curve. This latter model, which assumes variable surface enthalpy, best described our observations. The horizontal gray line indicates the Δ_rH° for bulk gypsum, the solid vertical gray line represents the hypothetical surface areas where $\Delta_rH^\circ_{Bas}$ is at a minimum, and the dashed vertical gray line represents the hypothetical surface area where $\Delta_rH^\circ_{Bas} = \Delta_rH^\circ_{Gyp}$.

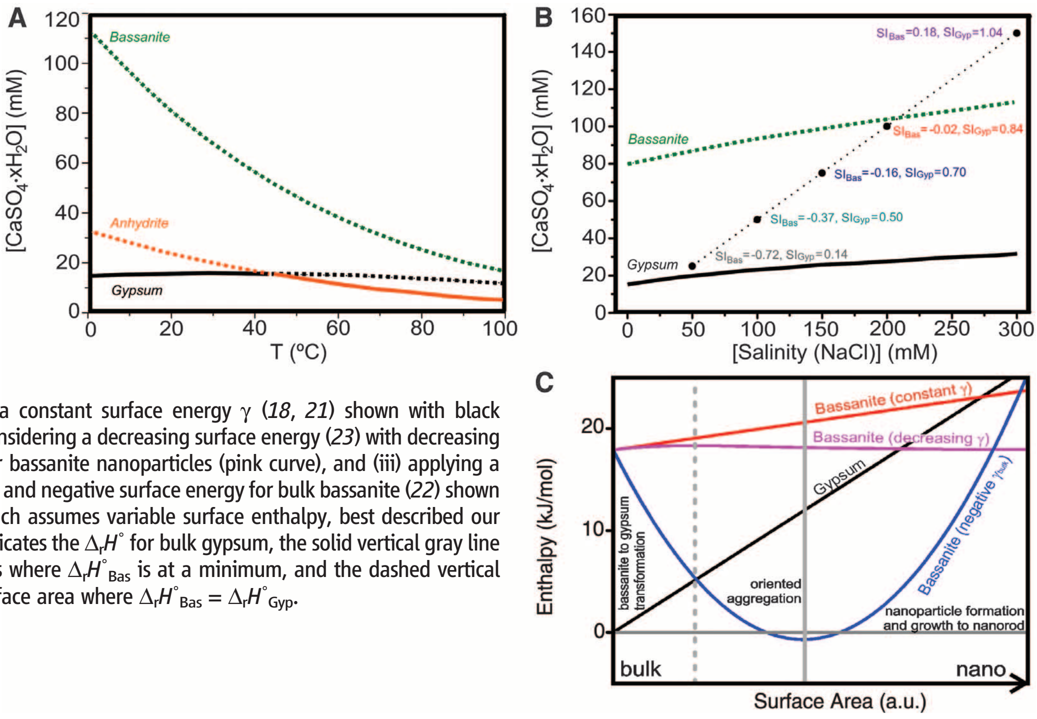

References and Notes

1. R. Buick, J. S. R. Dunlop, *Sedimentology* **37**, 247 (1990).
2. J. K. Warren, *Evaporites: Sediments, Resources and Hydrocarbons* (Springer-Verlag, Berlin, 2006).
3. Y. Langevin, F. Poulet, J. P. Bibring, B. Gondet, *Science* **307**, 1584 (2005).
4. J. J. Wray *et al.*, *Icarus* **209**, 416 (2010).
5. S. B. Ahmed, M. Tlili, M. B. Amor, H. B. Bacha, B. Elleuch, *Desalination* **167**, 311 (2004).
6. B. Mi, M. Elimelech, *Environ. Sci. Technol.* **44**, 2022 (2010).
7. N. B. Singh, B. Middendorf, *Prog. Cryst. Growth Charact. Mater.* **53**, 57 (2007).
8. Y. W. Wang, Y. Y. Kim, H. K. Christenson, F. C. Meldrum, *Chem. Commun.* **48**, 504 (2012).
9. J. D. Rodríguez-Blanco, S. Shaw, L. G. Benning, *Nanoscale* **3**, 265 (2011).
10. D. J. Tobler, S. Shaw, L. G. Benning, *Geochim. Cosmochim. Acta* **73**, 5377 (2009).
11. See supplementary materials on *Science* Online.
12. D. D. Wagman *et al.*, *J. Phys. Chem. Ref. Data* **11**, suppl. 2 (1982).
13. D. Freyer, W. Voigt, *Monatsh. Chem.* **134**, 693 (2003).
14. M. C. Ball, L. S. Norwood, *J. Chem. Soc. Faraday Trans. I* **74**, 1477 (1978).
15. L. Brečević, A. E. Nielsen, *J. Cryst. Growth* **98**, 504 (1989).
16. L. B. Gower, *Chem. Rev.* **108**, 4551 (2008).
17. A. Dey *et al.*, *Nat. Mater.* **9**, 1010 (2010).
18. J. M. McHale, A. Auroux, A. J. Perrotta, A. Navrotsky, *Science* **277**, 788 (1997).
19. M. R. Ranade *et al.*, *Proc. Natl. Acad. Sci. U.S.A.* **99** (suppl. 2), 6476 (2002).
20. A. Navrotsky, *Rev. Mineral.* **29**, 309 (1994).
21. A. Navrotsky, *Proc. Natl. Acad. Sci. U.S.A.* **101**, 12096 (2004).
22. Z. Lin, B. Gilbert, Q. Liu, G. Ren, F. Huang, *J. Am. Chem. Soc.* **128**, 6126 (2006).
23. H. Zhang, B. Chen, J. F. Banfield, *Phys. Chem. Chem. Phys.* **11**, 2553 (2009).
24. B. Winkler, B. Hennion, *Phys. Chem. Miner.* **21**, 539 (1994).
25. J. M. García-Ruiz, R. Villasuso, C. Ayora, A. Canals, F. Otálora, *Geology* **35**, 327 (2007).
26. A. E. S. Van Driessche, J. M. García-Ruíz, K. Tsukamoto, L. D. Patiño-Lopez, H. Satoh, *Proc. Natl. Acad. Sci. U.S.A.* **108**, 15721 (2011).

Acknowledgments: Supported by the Marie Curie EU-FP6 Mineral Nucleation and Growth Kinetics (MIN-GRO) Research and Training Network (contract MRTNCT-2006-035488), the School of Earth and Environment at the University of Leeds, the Consolíder-Ingenio 2010 project "Factoría Española de Cristalización," and project CGL2010-16882 of the Ministerio de Ciencia e Innovación (MICINN). We thank M. Ward, A. Brown, and S. Allshorn for help with sample preparation and characterization and three anonymous reviewers for their helpful comments.

Supplementary Materials

www.sciencemag.org/cgi/content/full/336/6077/69/DC1
Materials and Methods
Supplementary Text
Figs. S1 to S3
References (*27–35*)

24 October 2011; accepted 24 February 2012
10.1126/science.1215648

Late Accretion on the Earliest Planetesimals Revealed by the Highly Siderophile Elements

Christopher W. Dale,[1]* Kevin W. Burton,[1] Richard C. Greenwood,[2] Abdelmouhcine Gannoun,[3] Jonathan Wade,[4] Bernard J. Wood,[4] D. Graham Pearson[1,5]

Late accretion of primitive chondritic material to Earth, the Moon, and Mars, after core formation had ceased, can account for the absolute and relative abundances of highly siderophile elements (HSEs) in their silicate mantles. Here we show that smaller planetesimals also possess elevated HSE abundances in chondritic proportions. This demonstrates that late addition of chondritic material was a common feature of all differentiated planets and planetesimals, irrespective of when they accreted; occurring ≤5 to ≥150 million years after the formation of the solar system. Parent-body size played a role in producing variations in absolute HSE abundances among these bodies; however, the oxidation state of the body exerted the major control by influencing the extent to which late-accreted material was mixed into the silicate mantle rather than removed to the core.

Highly siderophile (iron-loving) elements [(HSEs): Re, Os, Ir, Ru, Rh, Pt, Pd, and Au] have low-pressure metal-silicate partition coefficients that are extremely high (10^7 to 10^{15}) (*1, 2*). Consequently, these elements should have been substantially partitioned into the metallic cores of Earth and other rocky planets, leaving their silicate mantles effectively stripped of HSEs. Yet the concentrations of the HSEs in Earth's upper mantle (*3*) and the martian mantle (*4, 5*) are much greater than predicted from low-pressure experimental data (Fig. 1, inset) (*6*). The siderophile behavior of some HSEs may, however, be greatly reduced under high pressure-temperature conditions, and on this basis it has been suggested that high-pressure equilibration at the base of a deep molten silicate layer, or magma ocean (*7, 8*), may account for their abundances in Earth's mantle. Nevertheless, the large apparent range of partition coefficients for HSEs, even at the elevated temperatures accompanying higher pressures in larger bodies (*9–11*), is not consistent with the chondritic (i.e., primitive solar system) patterns of HSEs in both the terrestrial and martian mantles or with the similarities in absolute abundances between the two bodies (*12*). This strongly suggests that high-pressure equilibration was not the dominant process controlling their present concentrations.

The simplest explanation of both the absolute and relative abundances of HSEs in the terrestrial and martian mantles is the late accretion of chondritic material after core formation, with material being mixed into the mantle by convection (*13, 14*). Chondritic late addition of between 0.4 and 1% of the mass of the terrestrial and martian mantles (*12*) is permitted by current dynamical models of planetary accretion. However, the Moon poses a problem because, despite its smaller cross section and much weaker gravitational field, its HSE concentrations (*15, 16*) are markedly lower than predicted by a late-accretion hypothesis (*12*). Stochastic late accretion offers a solution to this problem, with late-stage material provided by impactors drawn from a leftover planetesimal population dominated, in mass terms, by large bodies (*17*). With such a population, a limited number of massive random impacts could have delivered proportionally more material to Earth and Mars than to the much smaller Moon.

The accretionary histories of Vesta and similar asteroids were different from those of the terrestrial planets and the Moon, which accreted over time scales of 30 to 140 million years (My) (*4, 18*). The smaller asteroids appear to have experienced rapid, efficient, and relatively low-pressure metal-silicate equilibration during global-scale melting (*19*) within the first few million years of the solar system, with a relatively short time window for late accretion between the end of core formation and the crystallization of the magma ocean or crust (*18*). Given the short time scale, and a relative deficit of small planetesimals available to be accreted (*17, 20*), it is reasonable to predict that the silicate portions of these planetesimals possess extremely low HSE abundances, potentially with fractionated relative proportions reflecting equilibration during core formation, without substantial late addition of chondritic material.

Here we present HSE abundances and ^{187}Os/^{188}Os isotope data (*21*) for basaltic meteorites: the eucrites and diogenites [part of the howardite-eucrite-diogenite (HED) suite generally believed, and assumed here, to sample the asteroid 4 Vesta]; anomalous eucrites [considered to be from distinct Vesta-like parent bodies on the basis of their oxygen isotope compositions (*22*)]; angrites (from an unidentified parent body); and SNCs (believed to be from Mars).

Initial assessment of our data indicates that all the basaltic meteorites studied here have HSE interelement ratios (and Os isotope ratios) approaching those of chondrites (Fig. 1A and fig. S1), with some enrichment in Pt, Pd, and Re. There is no evidence for the extreme mantle depletions of Pt and Ir expected to accompany low-pressure metal-silicate equilibration (*1, 6*). The

---

[1] Department of Earth Sciences, Durham University, Durham DH1 3LE, UK. [2] Planetary and Space Science Research Institute, Open University, Walton Hall, Milton Keynes MK7 6AA, UK. [3] Laboratoire Magmas et Volcans, OPGC, UBP, UMR 6524, 5 Rue Kessler, 63038 Clermont Ferrand Cedex, France. [4] Department of Earth Sciences, University of Oxford, Parks Road, Oxford OX1 3PR, UK. [5] Department for Earth and Atmospheric Sciences, University of Alberta, Edmonton T6G 2E3, Canada.

*To whom correspondence should be addressed. E-mail: christopher.dale@durham.ac.uk